

Studies of Electron Cloud Growth and Mitigation in a Field Free Environment Using Retarding Field Analyzers

J.R. Calvey, G. Dugan, W. Hartung, J.A. Livezey, J. Makita, M.A. Palmer
CLASSE, Cornell University, Ithaca, NY, USA

(Dated: April 28, 2013)

In 2008, the Cornell Electron Storage Ring (CESR) was reconfigured to serve as a test accelerator (CESRTA) for next generation lepton colliders, in particular for the ILC damping ring. A significant part of this program has been the installation of diagnostic devices to measure and quantify the electron cloud effect, a potential limiting factor in these machines. In particular, several Retarding Field Analyzers (RFAs) have been installed in CESR. These devices provide information on the local electron cloud density and energy distribution, and have been used to evaluate the efficacy of different cloud mitigation techniques. This paper will provide an overview of RFA results obtained in a field free environment. Understanding these results through the use of specially modified cloud buildup simulations provides a great deal of insight into the behavior of the electron cloud, strengthens the validity of the model used in the analysis, and provides essential information on the electronic properties of the chamber surface of immediate and direct applicability to other storage rings.

PACS numbers:

I. INTRODUCTION

The electron cloud effect is a well known phenomenon in particle accelerators (see, for example, [1]), in which a high density of low energy electrons builds up inside the vacuum chamber. These electrons can cause a wide variety of undesirable effects, including emittance growth and beam instabilities. The cloud can be seeded by photoelectrons generated by synchrotron radiation, or by ionization of residual gas. The collision of these “primary” electrons with the beam pipe can then produce one or more (“secondary”) electrons, depending on the secondary electron yield (SEY) of the material. If the average SEY is greater than unity, the cloud density will grow exponentially, until a saturation is reached.

Electron cloud has been observed in many existing facilities (including, for example, PEP-II [2], CERN SPS [3], KEKB [4], ANL APS [5], FNAL Main Injector [6], and the LHC [7]), and is expected to be a major limiting factor in next generation storage rings. It is of particular concern in the damping rings of electron-positron colliders, which will produce a large amount of synchrotron radiation and require very small emittances [8].

In 2008, the Cornell Electron Storage Ring (CESR) was reconfigured to study issues related to the design of International Linear Collider (ILC) damping ring, including electron cloud. A significant component of this program, called CESR Test Accelerator (CESRTA) was the installation of several retarding field analyzers (RFAs) throughout the ring, in drift, dipole, quadrupole, and wiggler field regions. This paper will summarize results obtained from drift RFAs. More specifically, it will describe the design of the RFAs and the experimental sections in CESR where they were installed (Section II); present measurements (Section III), with a focus on directly comparing different cloud mitigation techniques;

describe a method for modeling the RFAs in cloud simulation programs (Section IV); and give detailed results from these simulations (Section V).

The combined analysis of measurements and simulations allows us to characterize electronic properties (photoemission and secondary emission) of the surface of many portions of the vacuum chamber without resorting to external measuring devices. This process has the virtue that all surface conditioning effects due to the beam are intrinsically taken into account. Additionally, by comparing data and simulation on a detailed level we have substantially validated the electron emission model embodied in the simulation codes, and therefore reinforced our confidence in their applicability in other situations, in particular to hadron storage rings. Finally, we have been able to study several mitigation techniques in detail, and evaluate their effectiveness in preventing electron cloud build-up.

A. Retarding Field Analyzers

A retarding field analyzer consists of three main components [9]: holes drilled in the beam pipe to allow electrons to enter the device; a “retarding grid,” to which a voltage can be applied, rejecting electrons with less than a certain energy; and a positively biased collector, to capture any electrons which make it past the grid (Fig. 1). If space permits, additional (grounded) grids can be added to allow for a more ideal retarding field. In addition, the collectors of most RFAs used in CESRTA are segmented to allow characterization of the spatial structure of the cloud build-up. Thus a single RFA measurement provides information on the local cloud density, energy, and transverse distribution. Most of the data presented here are one of two types: “voltage scans,” in which the retarding voltage is varied (typically from +100 to -250 V

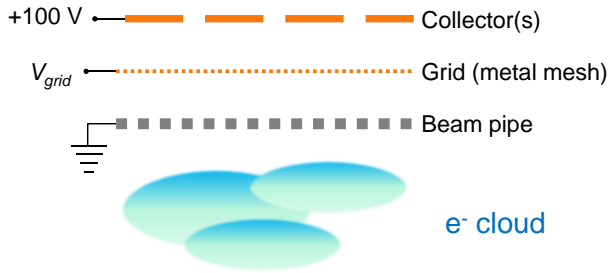


FIG. 1: Idealized diagram of a retarding field analyzer.

or -400 V) while beam conditions are held constant, or “current scans,” in which the retarding grid is set to a positive voltage (typically $+50$ V), and data are passively collected while the beam current is increased. The collector was set to $+100$ V for all of our measurements.

The use of RFAs for electron cloud studies was pioneered at APS [9]; additional studies have been performed at the FNAL Main Injector [10], PEP-II [11], and KEKB [12]. However, the CESR-TA RFA program is unprecedented in terms of scale. We have used RFAs to probe the local behavior of the cloud at multiple locations in CESR, under many different beam conditions, and in the presence of several different mitigation schemes.

B. CESR Parameters

The primary advantage of CESR as a test accelerator is its flexibility. At CESR-TA, we have been able to study the behavior of the electron cloud as a function of several different beam parameters, varying the number of bunches, bunch current, bunch spacing, beam energy, and species. As will be described in Section V, this is very helpful for independently determining the photoelectron and secondary electron properties of the instrumented chambers. Table I gives some of the basic parameters of CESR, and lists some of the beam parameters used for electron cloud mitigation studies with RFAs. A more complete description of the full operating range of CESR can be found in [13].

C. Cloud Mitigation

In addition to solenoid windings (which trap electrons near the vacuum chamber wall [2]), the primary method of reducing electron cloud density in a field free region is the use of beam pipe coatings, which reduce the primary and secondary emission yield of the chamber. Coatings tested at CESR-TA include titanium nitride (TiN) [14], amorphous carbon (aC) [3], diamond-like carbon (DLC) [15], and Ti-Zr-V non-evaporable getter (NEG) [16].

TABLE I: CESR parameters and typical beam conditions for electron cloud mitigation studies

Parameter	Value(s)	Units
General Parameters		
Circumference	768	m
Revolution Period	2.56	μ s
Harmonic number	1281	-
Number of bunches	9, 20, 30, 45	-
Bunch spacing	4 - 280	ns
Beam energy	2.1, 4, 5.3	GeV
2.1 GeV Parameters		
RMS Horizontal Emittance	2.6	nm
RMS Vertical Emittance	.02	nm
RMS Bunch Length	12.2	mm
Bunch current	0 - 5	mA ^a
Beam species	e^+ , e^-	-
4 GeV Parameters		
RMS Horizontal Emittance	23	nm
RMS Vertical Emittance	.23	nm
RMS Bunch Length	9	mm
Bunch current	0 - 6	mA
Beam species	e^+	-
5.3 GeV Parameters		
RMS Horizontal Emittance	144	nm
RMS Vertical Emittance	1.3	nm
RMS Bunch Length	20.1	mm
Bunch current	0 - 10	mA
Beam species	e^+ , e^-	-

^a1 mA = 1.6×10^{10} particles

II. INSTRUMENTATION

RFA measurements have been a part of the CESR-TA program since it began in mid 2008. A more detailed description of the design and construction of the RFAs and experimental sections can be found in [17]; here we provide a brief overview.

There are five main electron cloud experimental sections of CESR instrumented with drift RFAs. These include long sections freed up by the removal of the wigglers at Q14E and Q14W (the names refer to their proximity to the 14E and 14W quadrupoles, respectively), shorter sections at Q15E and Q15W, and a long straight section at L3. The vacuum chambers at Q15E/W are approximately elliptical and made of aluminum (as is most of CESR), while the chambers at Q14E/W are rectangular and made of copper, and the pipe is circular stainless steel at L3. Fig. 2 shows the locations of these experimental sections in the CESR ring.

A. Q14W and Q14E Test Sections

Upon the removal of the CESR-c superconducting wigglers, two electron cloud experimental sections were created on both east and west arcs of CESR. Measurements in the Q14W test section confirmed that an “Insertable I” style RFA gives results comparable to the well un-

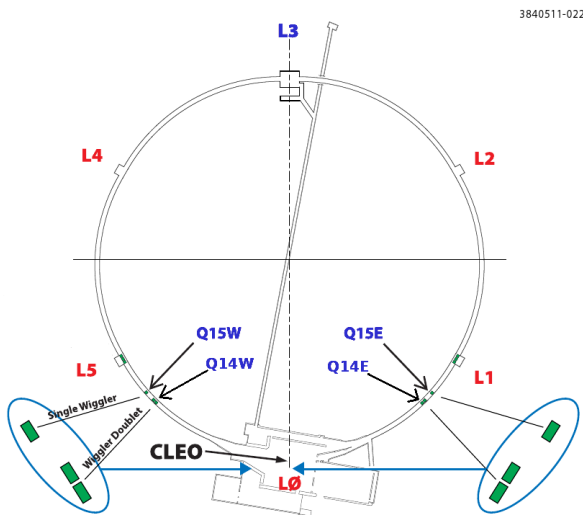


FIG. 2: The reconfiguration of the CESR vacuum system provided space for several electron cloud experimental sections. Drift RFAs are located at Q14E/W, Q15E/W, and L3.

derstood “APS” style [18] (see below for descriptions of the different RFA styles). At Q14E, the copper beam pipe was coated with TiN thin film for half of its length (while the other half remained bare copper). Insertable RFAs were installed at each end of this test chamber to compare electron cloud intensity in the two sections.

B. Q15W and Q15E Mitigation Comparison Chambers

To allow for frequent exchange of the test chambers while minimizing the impact on the accelerator operations, two very short experimental regions were created in the Q15W and Q15E locations in the arcs. Over the course of the CESRTA program, four chamber surfaces were tested in these locations: bare aluminum (as it was originally extruded), aC coatings (coated by CERN/CLIC), TiN coating (by Cornell) and DLC coating (by KEK). Table II gives detailed information on these chambers, and Fig. 3 shows a typical installation at Q15W.

There is some evidence the aC coated chambers may have been contaminated by silicone tape present during the bakeout of the chamber [17], raising the effective SEY. However, as described in Section III, these chambers still showed good performance in situ.

C. L3 Test Section

A Ti-Zr-V non-evaporable getter (NEG) thin film [16] has been shown to have a low SEY, after its activation at elevated temperatures under vacuum. The activated NEG coating also has the benefit of providing vacuum

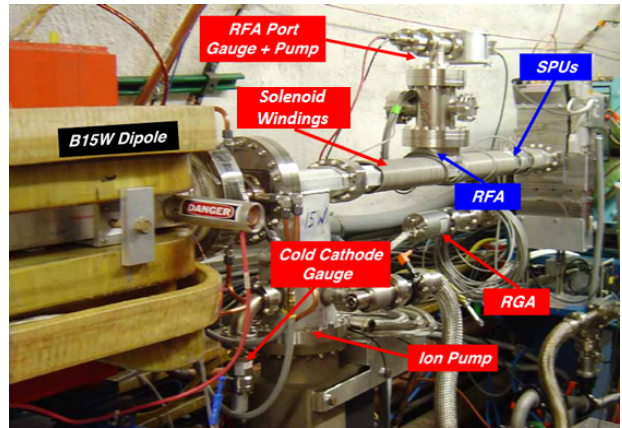


FIG. 3: A Q15 experimental chamber installed at Q15W in CESR. In addition to the RFA, the chamber contains 4 shielded pickups (SPUs) [19].

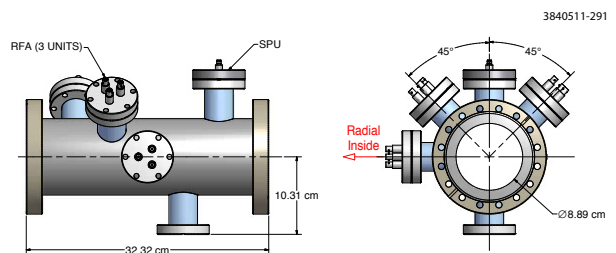


FIG. 4: Electron cloud diagnostic chamber with NEG thin film coating.

pumping. A NEG-coated test chamber was built and tested in the drift section of the L3 experimental region in CESR. To prevent rapid saturation of the activated coating from residual gases in the surrounding beam pipes, the test chamber was sandwiched between two 1-m long NEG coated beam pipes. The chamber was equipped with three APS-style RFAs at three different azimuthal angles (see Fig. 4). All three chambers were made of stainless steel (Type 304L).

D. RFA Styles

Several different styles of RFA have been deployed throughout drift sections in CESR. Table III summarizes the key parameters of each style, and Table IV describes the different types of grids used. A more detailed description of each RFA style follows:

a. “Thin test” style The “thin test” style RFA was designed to test whether RFAs could perform in vacuum chambers where detector space is severely limited due to magnet apertures, and to serve as a stepping stone to the more complex models described below. It consists of a single grid and single collector, spaced by 1 mm. A self supporting stainless steel grid with an etched bi-conical hole structure (.18 mm diameter holes with a .25 mm

TABLE II: Summary of Q15W and Q15E Experimental Vacuum Chambers (VCs)

VC	Surface	Run	RFA Style	Test Period	Location	Note
1	Al	1	Thin	Jul 2009-Nov 2009	E	Reference surface
		2	Thin	Apr 2010-Aug 2010	W	
		3	Insertable II	Aug 2012-present	E	
2	TiN	1	Thin	Dec 2009-Apr 2010	E	Coated by DC sputtering at Cornell
		2	Thin	Aug 2010-Jan 2011	W	
		3	Insertable II	Feb 2011-Jul 2011	W	
		4	Insertable II	Aug 2012-present	W	
3	aC	1	Thin	Jul 2009-Apr 2010	W	Coated by DC sputtering at CERN
4	aC	1	Thin	Apr 2010-Jan 2011	E	Coated by DC sputtering at CERN
		2	Insertable II	Jul 2011-Jul 2012	W	
5	DLC	1	Insertable II	Feb 2011-Jul 2012	E	Coated by pulsed DC chemical vapor deposition, supplied by KEK

TABLE III: Drift RFA styles deployed in CESR. Each RFA has one retarding grid. For RFAs with multiple grids, the additional grids are grounded.

Type	Grids	Collectors	Grid Type
Thin Test	1	1	Etched
APS	2	1	Mesh
Insertable I	2	5	Etched
Insertable II	3	11	HT Mesh
Thin	1	9	HT Mesh

TABLE IV: Grid types used in CESR RFAs. Note that “transparency” refers to the optical transparency.

Type	Transparency	Material	Thickness
Etched	40%	Gold coated SST	150 μm
Mesh	46%	SST	76 μm
HT Mesh	90%	Copper	13 μm

pitch) was chosen for the grid. In addition, the grid layer was vacuum-coated with a thin gold layer (several hundred nm) to reduce its secondary electron yield. The electron collector pad was laid out on copper-clad Kapton sheet using standard printed circuit board fabrication techniques.

b. APS style This design is based on a well understood style of RFA [9], and was used as a cross check to verify reasonable operation of the “Insertable I” style, described below. It consists of a single collector, and two stainless steel meshes for grids. APS style RFAs were also deployed in the L3 NEG test chamber (Section II C).

c. Insertable I Deployed in the Q14E and Q14W experimental regions of CESR, these RFAs were designed to be “inserted” on top of a standard vacuum chamber. They have two stainless steel grids, spaced by 3 mm. Transverse resolution is provided by five (Kapton) collectors. Holes are drilled in the beam pipe in five segments; each segment has 25 holes, with diameter 1.5 mm

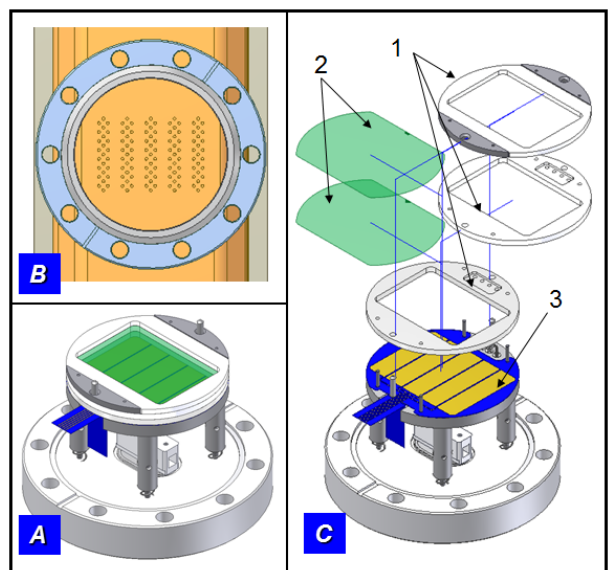


FIG. 5: Engineering diagram of an “Insertable I” style RFA. (A) Assembled RFA structure. (B) Vacuum chamber hole pattern. (C) Exploded view of the RFA, showing (1) Macor spacers, (2) stainless steel grids, and (3) flexible circuit collectors.

and depth 5.1 mm. The dimensions of the RFA holes are chosen to ensure no significant leakage of the beam’s RF fields into the detector signals, while maximizing the transparency of the RFA to the vacuum chamber. Fig. 5 gives a detailed picture of this RFA.

d. Thin style Designed for use inside a CESR dipole, where aperture space is limited, the thin style detector was also used in the Q15E and Q15W drift sections. The RFA housing is machined from a separated block of explosion-bonded aluminum-to-stainless steel material, and is welded to the cutout on top of the beam pipe. The lower face of the RFA housing matches

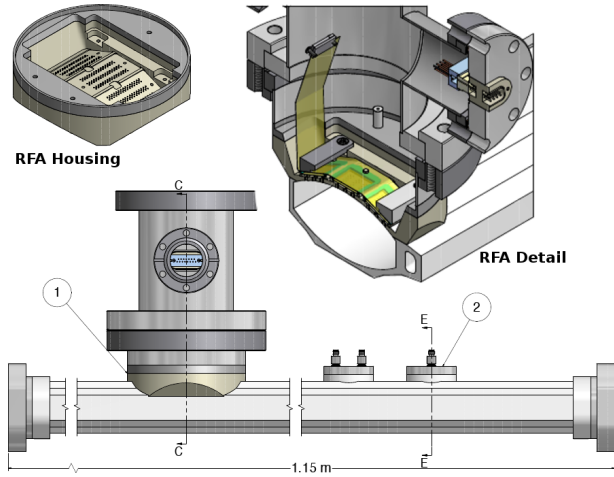


FIG. 6: Q15 EC Test Chamber, equipped with an RFA (1) and 4 shielded pickups (2)

the curvature of the beam pipe aperture, while the upper face is divided into three flat sections. Each section has one retarding grid, which is made of high efficiency electro-formed copper mesh, held in place by a stainless steel frame. There are three collectors in each section, for a total of nine. The total distance from the outside of the vacuum chamber to the collectors is 2.5 mm. The beam pipe holes are 0.75 mm in diameter and ~ 2.5 mm in thickness, maintaining the same ratio of diameter to thickness used for the “Insertable I” style. There are 44 holes per collector. A diagram of a Q15 test chamber, which includes a thin RFA (as well as 4 shielded pickup detectors [19]) is shown in Fig. 6.

e. Insertable II The second generation insertable RFA has three grids, consisting of high-transparency copper meshes, spaced by 5.7 mm. The retarding voltage is applied to the middle grid. Insertable II RFAs were installed in the 5th Q15 test chambers, replacing the “thin” style detectors. The additional grids and increased spacing between them results in a more ideal retarding field, and reduces some of the troublesome complications observed in the “thin” RFA (see Section IV). It also allows for higher retarding voltage, up to -400 V. To provide cross calibration between the two RFA designs, a TiN-coated test chamber in Q15W was instrumented with both styles (refer to Table II).

E. Data Acquisition System

A modular high voltage power supply and precision current monitoring system has been designed to support simultaneous RFA measurements at multiple locations around CESR [18]. Data acquisition is controlled through a MATLAB based graphical user interface, which also allows for real time monitoring and control of any RFA. Data are collected simultaneously by all the RFAs, and the GUI allows for commands to be issued

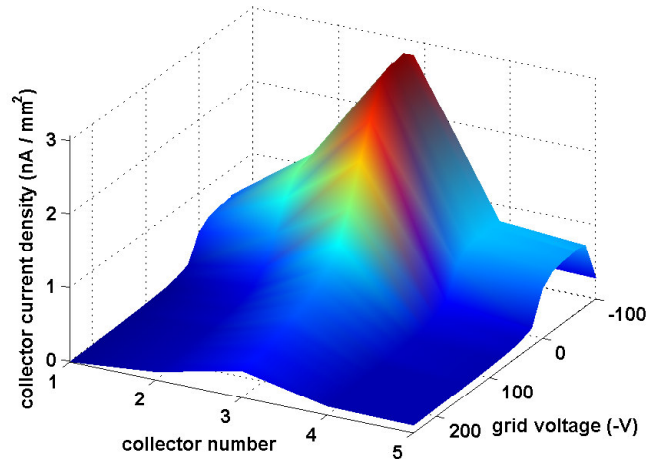


FIG. 7: RFA voltage scan with an “Insertable I” style drift RFA in a Cu chamber, 1x45x1.25 mA e^+ , 14 ns, 5.3 GeV

to all the devices at once.

III. MEASUREMENTS

Many of our earliest detailed measurements were done with “Insertable I” style RFAs (Table III). Fig 7 shows an example of a voltage scan done with one of these detectors, in typical CESR-TA beam conditions. The RFA response is plotted as a function of collector number and retarding voltage. Roughly speaking, this is a description of the transverse and energy distribution of the cloud. Collector 1 is closest to the outside of the chamber (where direct synchrotron radiation hits); the central collector (3 in this case) is aligned with the beam. The sign convention for retarding voltage is chosen so that so a positive value on this axis corresponds to a negative physical voltage on the grid (and thus a rejection of lower energy electrons). In this example, the signal is fairly broad across all five collectors, indicating that the cloud density is not strongly peaked around the beam. It also falls off quickly with retarding voltage, indicating that the majority of cloud particles have low energy. The RFA signal is expressed in terms of current density in nA/mm^2 , normalized to the transparency of the RFA beam pipe and grids. In principle, this gives the time averaged electron current density incident on the beam pipe wall. The beam conditions are given as “1x45x1.25 mA e^+ , 14 ns, 5.3 GeV.” This notation, which will be used throughout this section, indicates one train of 45 bunches, with 1.25 mA/bunch ($1 \text{ mA} = 1.6 \times 10^{10}$ particles), with positrons, 14 ns spacing, and at beam energy 5.3 GeV.

As described in Section IID, both “thin” and “Insertable II” style RFAs have been installed at Q15E and Q15W. Example measurements done with both of these RFA styles, in a TiN-coated chamber, can be found in

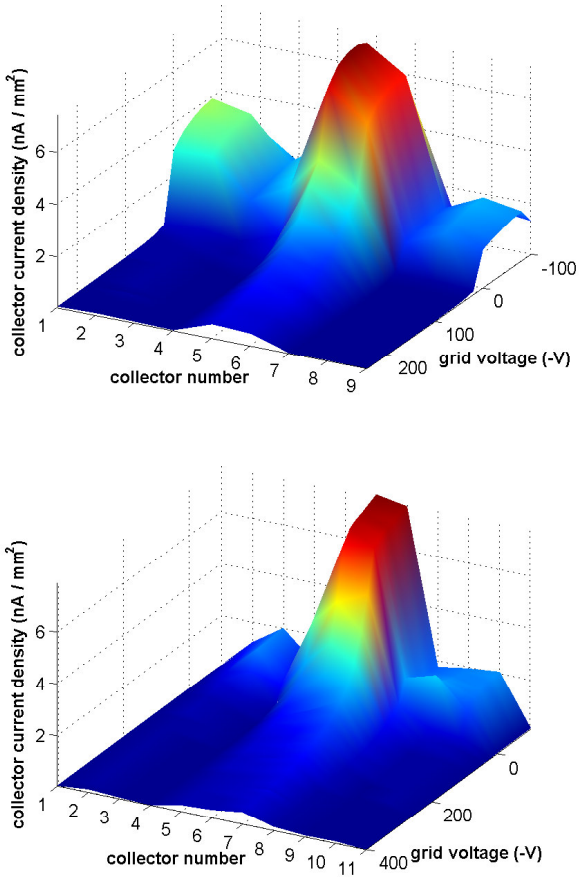


FIG. 8: Example voltage scans with thin (top) and Insertable II (bottom) style drift RFAs in the same location (Q15W). Both are TiN-coated, beam conditions are $1 \times 45 \times 1.25$ mA, 5.3 GeV, 14 ns.

Fig. 8. These measurements can be contrasted with one done at higher bunch current (Fig. 9). Here we observe the signal extends to much higher energy, and is more strongly peaked in the central collector.

A. Bunch Spacing Comparison

Although our RFA measurements are not time resolved, we can probe the time scale of cloud development by examining the RFA response as a function of bunch spacing, which can be varied in 4 ns increments. Fig. 10 shows such a comparison for the Q15W aC coated RFA. We observe that the signal at high retarding voltage (i.e. the number of high energy cloud particles) is highest for the 4 ns data, and falls off quickly and monotonically with increasing bunch spacing. With short bunch spacing, a typical electron will receive multiple beam kicks before colliding with the vacuum chamber, gaining 100s of eV in the process. However, the total signal (including high and low energy electrons) is actually highest

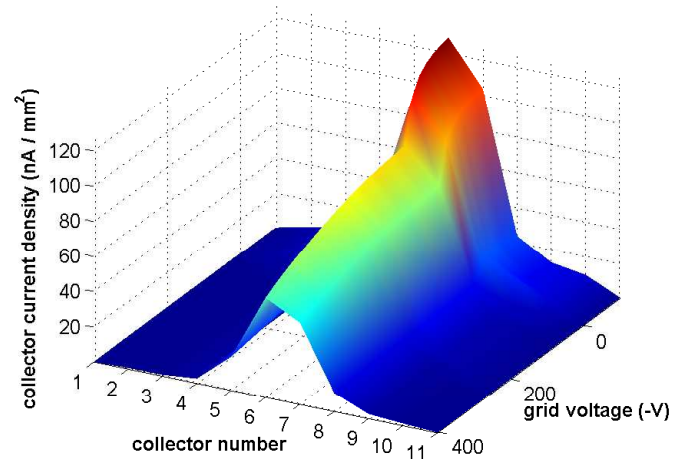


FIG. 9: Voltage scan at high bunch current, $1 \times 20 \times 10$ mA e^+ , 5.3 GeV, 14 ns, Insertable II RFA, in a TiN-coated chamber at Q15W.

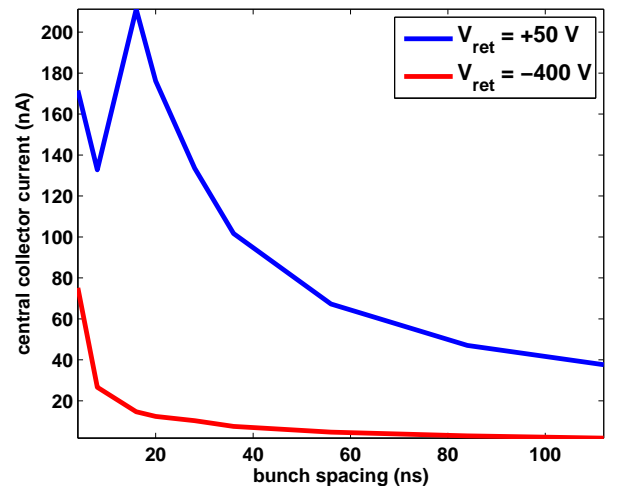


FIG. 10: Central collector signal as a function of bunch spacing, $1 \times 20 \times 3.6$ mA e^+ , 5.3 GeV, in an aC coated chamber at Q15W.

for 16 ns. This is consistent with a multipacting resonance [20, 21], in which the kick from the beam gives secondary electrons near the vacuum chamber wall just enough energy to reach the opposite wall in time for the next bunch. These electrons generate more secondaries, which are again given energy by the beam. This process continues, resulting in a resonant buildup of the cloud. The resonant condition is $t_b = \frac{r^2}{cr_e N_b}$, where t_b is the bunch spacing, r is the chamber half-height, r_e is the classical electron radius, and N_b is the bunch population. For the beam conditions in Fig. 10, this comes out to 13 ns, consistent with the 16 ns peak observed.

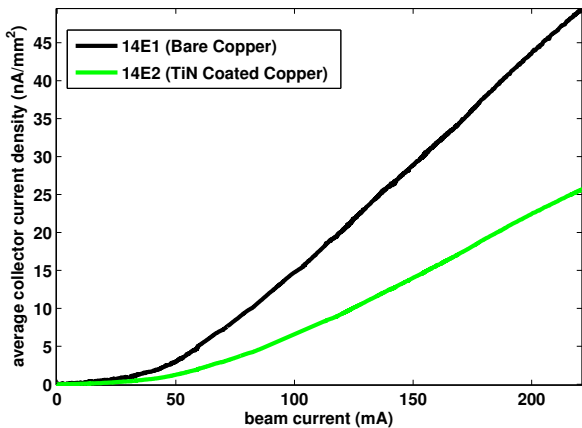


FIG. 11: Comparison of insertable drift RFAs, 1×20 e⁺, 5.3 GeV, 14 ns

B. Mitigation Comparisons

An important component of the CESR-TA program is the direct comparison of different electron cloud mitigating coatings, tested at Q14E, Q15E/W, and L3. In this section we compare “current scans” (RFA signal as a function of beam current), for different mitigations in each of the instrumented sections of CESR. The transverse distribution observed at a given beam current was substantially the same for different chambers, so the plots shown below average over the RFA collectors. All of the measurements were done with the retarding grid biased to +50 V in order to measure cloud electrons of all energies.

1. Comparison of adjacent chambers at Q14E

Fig. 11 compares a current scan measurement done simultaneously with two adjacent RFAs in the Q14E section (Section II A), one in a bare copper chamber, and one in a TiN-coated copper chamber. Here we compare the average collector current density in the two detectors, as a function of beam current, and find that it is lower in the coated chamber by a factor of two. The photon flux is actually about 50% higher in the TiN coated chamber, so a more direct comparison would show an even larger improvement.

2. Comparisons of chambers with different coatings installed at the same locations at Q15E/W

The majority of our mitigation studies were done with RFAs in the Q15W and Q15E experimental sections (Section II B). The photon flux from a positron beam at Q15W is about twice that of Q15E, and vice versa for an electron beam. Measurements have been taken at

both locations with TiN and aC coatings, as well as with an uncoated aluminum chamber (see Table II). In addition, a chamber with DLC coating has been installed at Q15E. By comparing measurements taken at the same location in CESR, we ensure the comparisons can be made under identical beam conditions, including photon flux. Figs. 12 through 14 compare the RFA signal with each of these coatings for typical sets of CESR-TA beam conditions. The beam energy is 5.3 GeV in all cases; the comparisons are for one train of 20 bunches spaced by 14 ns (positrons in Fig. 12, electrons in Fig. 13) and 9 bunches of positrons spaced by 280 ns (Fig. 14). We have generally found that data taken with 20 bunches of positrons at high current shows the biggest difference between the different chambers. It is under these conditions that we expect to be most sensitive to the secondary electron yield.

There was some concern that these measurements could be affected by the adjacent aluminum chambers (which should have a higher cloud density). To address this issue, 100 Gauss dipole magnets were installed on either side of the coated chambers, to prevent longitudinal motion of electrons into the chambers. We found that the use of these magnets had little effect on the RFA measurements.

All coated chambers show a sizeable reduction in signal when compared to uncoated aluminum. We have found that exposure to electron cloud bombardment significantly improved the performance of the TiN-coated chamber. This effect, known as “scrubbing” or “processing,” is well known [22], and has been observed in direct measurements of the SEY of a TiN coated chamber [14]. In these plots, “unprocessed” TiN refers to data taken after 2.5 A-hrs of beam processing, while the “processed” chamber received 940 A-hrs. The aC chamber’s signal was initially low, and we did not observe a significant change in signal with EC bombardment. After extensive processing of the TiN chamber, TiN and aC showed similar mitigation performance.

At first glance, it appears DLC may perform better than other coatings at very high beam current. However, it should be noted that bench measurements of the Secondary Electron Yield (SEY) of DLC have found that the material can retain charge if bombarded with a sufficiently high electron flux, thus modifying the apparent SEY performance [23]. This effect may also be influencing the in situ measurements presented here. Evidence for this theory can be found in Fig. 15, which compares a voltage scan done at high beam current in a DLC and aC chamber. The aC shows an enhancement at positive retarding voltage, which is seen in almost all of our drift RFA data (see Section IV). The DLC chamber instead shows a nonphysical spike at 0 V, but no enhancement at positive voltage. This could be the result of charge around the beam pipe holes influencing the transmission of low energy electrons.

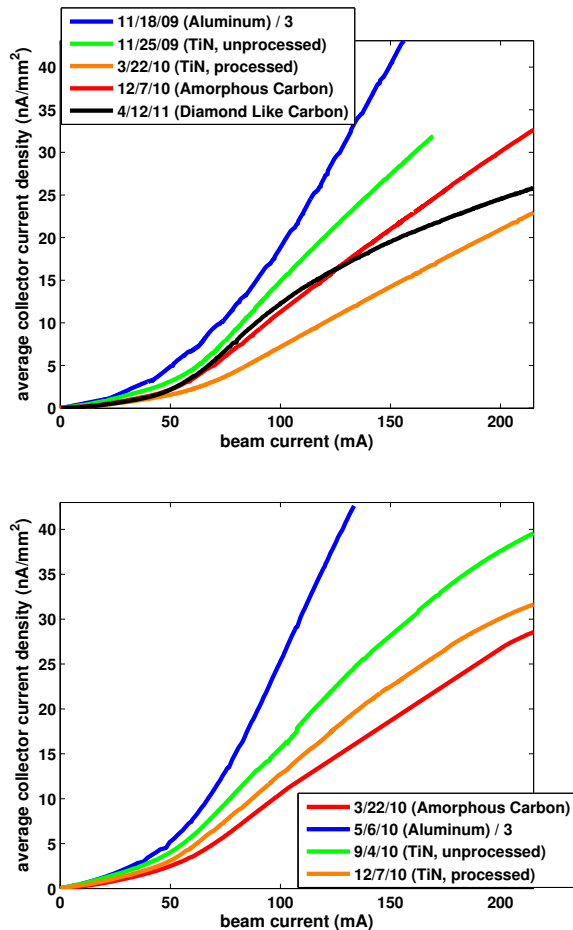


FIG. 12: Comparison of different beam pipe coatings, Q15E (top), and Q15W (bottom) drift RFAs. Plots show average collector signal vs beam current for 20 bunches of positrons with 14 ns spacing, at beam energy 5.3 GeV. Note that the aluminum chamber signals are divided by 3.

3. Long Term Behavior

Another important issue addressed by the CESR RFA measurements is the long term reliability of various chambers and coatings. Figures 12 - 14 show that significant processing was observed in TiN-coated chambers in both Q15E and Q15W; this was not observed in the aC chambers. However, more recent measurements (Fig. 16) have shown some processing in an aC coated chamber. While reduction of the secondary yield has not been observed in aC, this decrease in signal could be explained by a reduction in the quantum efficiency [24]. This effect was not observed in the other aC data, most likely because RFA measurements were not made soon enough after installation.

The signal measured in the DLC chamber varied significantly over time (Fig. 17). Apart from some initial processing, the measurements in this chamber do not appear to show any obvious trend. It is possible that the properties of the DLC depend on the recent beam history

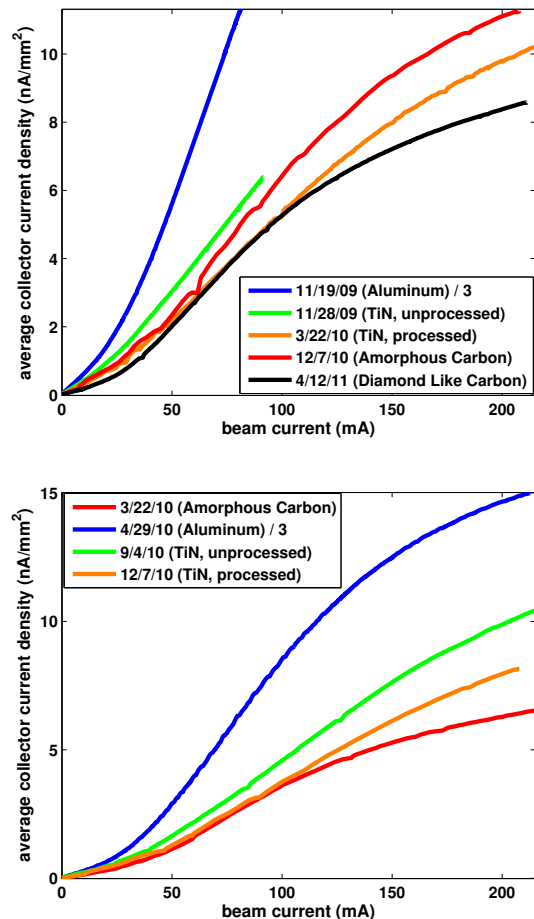


FIG. 13: Comparison of different beam pipe coatings, Q15E (top), and Q15W (bottom) drift RFAs. Plots show average collector signal vs beam current for 20 bunches of electrons with 14 ns spacing, at beam energy 5.3 GeV. Note that the aluminum chamber signals are divided by 3.

before the measurement.

4. Activation and processing of NEG coated chambers in L3

The performance of the L3 NEG coated chamber (Section IIC) has also been monitored using RFAs. Fig. 18 compares the current measured by one of these RFAs on several different dates, corresponding to different states of activation and processing of the NEG coating. It was observed that both activation and initial processing reduced the signal measured by this RFA. After a CESR down (during which the NEG was activated again), the signal rose somewhat, but it processed back down to its minimum value after a few months of beam time. The other two detectors showed a similar trend. These signals remained consistent in subsequent runs.

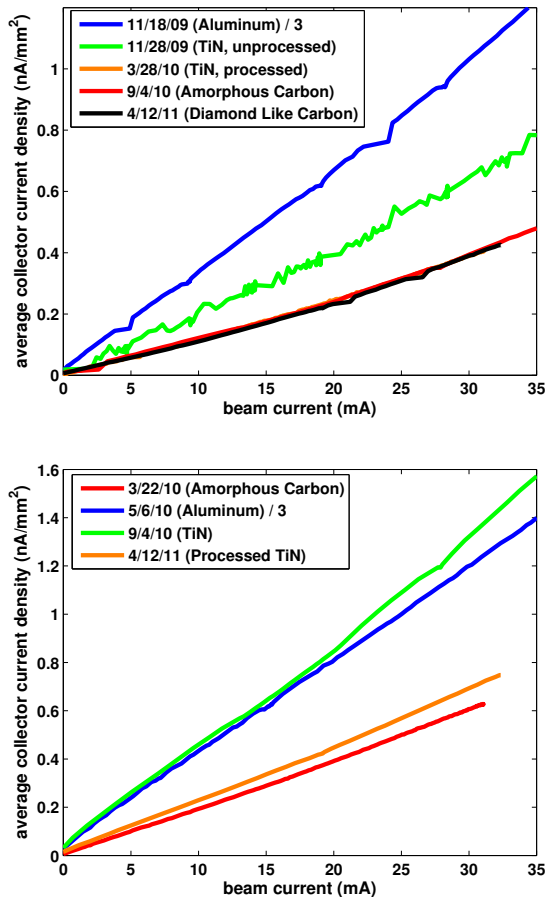


FIG. 14: Comparison of different beam pipe coatings, Q15E (top), and Q15W (bottom) drift RFAs. Plots show average collector signal vs beam current for 9 equally spaced (280 ns) bunches of positrons, at beam energy 5.3 GeV. Note that the aluminum chamber signals are divided by 3. In the top plot, the curve for processed TiN is difficult to see, because it lies almost directly under the curve for aC.

IV. RFA MODELING

To understand the measurements described above on a more fundamental level, we need a way of translating an RFA measurement into physical quantities relating to the development of the electron cloud. To bridge this gap, accurate models of both the cloud development and the RFA itself are required. The former task is handled by the well validated cloud simulation code POSINST [25–27], which tracks the motion of cloud particles during and after the passage of a bunch train. We have modified POSINST to include a model of the RFA, which automatically generates an output file containing the simulated RFA signals.

This integrated RFA model is implemented as a special function that is called when a macroelectron in the simulation collides with the vacuum chamber wall, immediately before the code section that simulates secondary

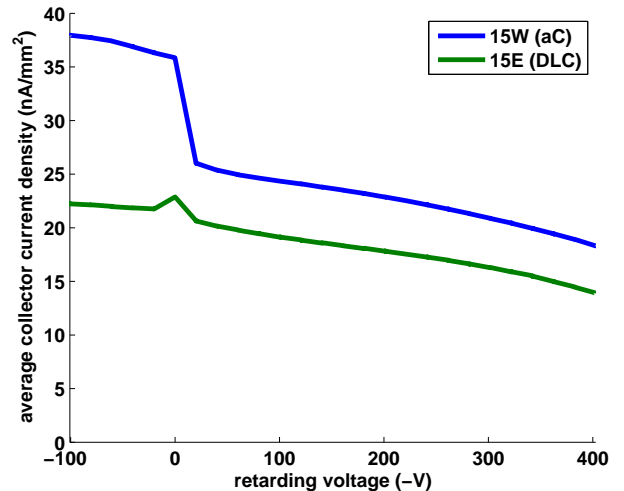


FIG. 15: Comparison of amorphous and diamond-like carbon at high beam current, $1 \times 20 \times 10 \text{ mA } e^+$, 5.3 GeV, 14 ns.

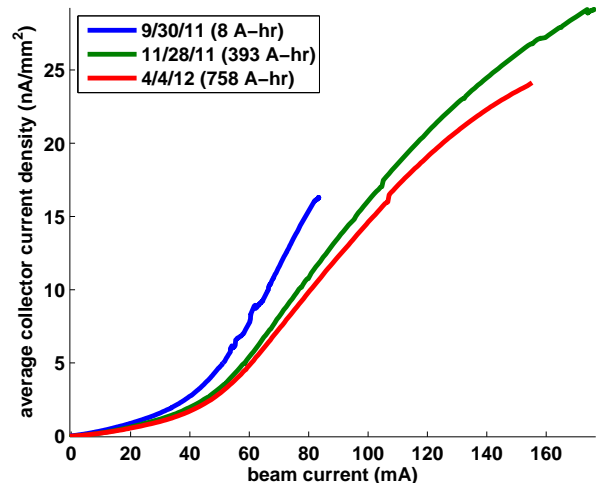


FIG. 16: Processing history in the newer Q15W aC coated chamber, $1 \times 20 e^+$, 5.3 GeV, 14 ns. Integrated beam doses are given for each measurement.

emission. First, this function checks if the macroelectron is in the region covered by the RFA. If so, a certain fraction of the particle’s charge, which depends on the incident angle and energy (as well as the overall beam pipe transparency), is added to the collector signal. The RFA acceptance as a function of angle and energy is calculated by a separate particle tracking code, described below. The charge is binned by energy and transverse position, reproducing the energy and position resolution of the RFA. The macroelectron then has its charge reduced by the amount that went into the detector, and the simulation continues as normal. This process is shown diagrammatically in Fig. 19.

In order for this method to work, we need to know the

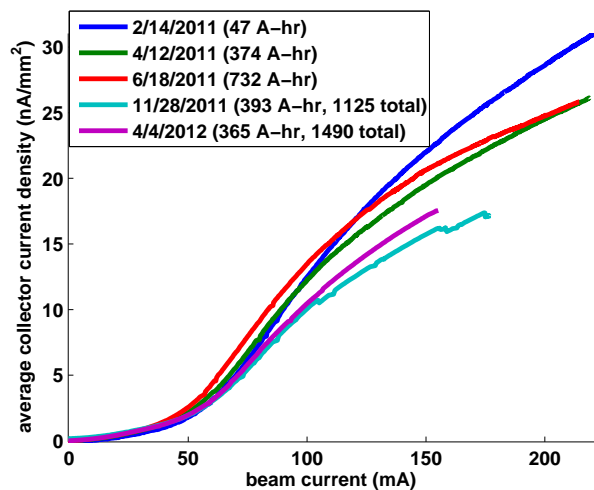


FIG. 17: Performance of Q15E DLC chamber over time, 1×20 e^+ , 5.3GeV, 14ns. Integrated beam doses are given for each measurement. Where two doses are shown, the first is counted from the last CESR down, and the second from the installation of the chamber.

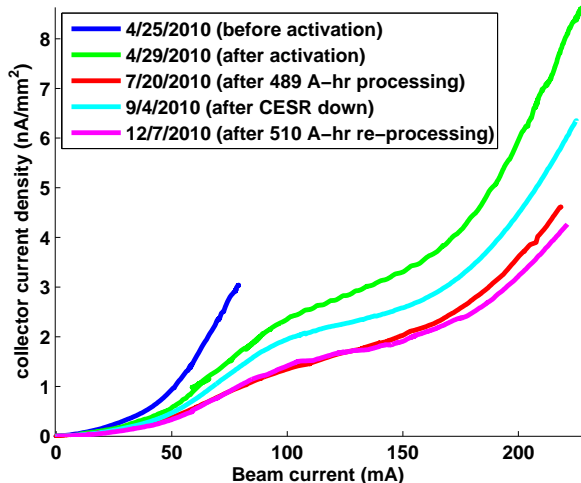


FIG. 18: NEG RFA comparison, 1×20 e^+ , 5.3GeV, 14ns

RFA response to a particle with a given incident energy and angle. To answer this question, we developed a specialized code, which tracks electrons through a model of the RFA. The model includes a detailed replica of the beam pipe, grid(s), and collector, as well as a realistic map of the electric fields inside the RFA, generated by the electrostatic calculation tool Opera 3D (Fig. 20). The tracking code also allows for the production of secondary electrons on both the beam pipe and grid(s). The secondary emission model is a simplified version of the one used in POSINST, and includes both elastic and “true” secondaries (see Section V A). The output of the simulation is a table which maps the incident particle energy and angle to both a “direct” and (low energy)

“secondary” collector signal. POSINST can then consult this table to determine the RFA response to a given macroelectron-wall collision.

The production of secondary electrons in the beam pipe holes and on the retarding grid is an especially important effect, and results in an enhanced low energy signal in most of our drift RFA measurements. Fig. 21 shows the simulated secondary signal in a thin style RFA, as a function of incident angle, for different incident electron energies. The effect is particularly strong for electrons with high energy and moderate angle.

To aid in the development of our model, we constructed a bench experiment to study the response of a test RFA under controlled conditions. The system consists of an electron gun, which can produce a monoenergetic and roughly uniform beam of electrons, aimed at a test RFA. The electron gun and RFA are installed in a vacuum chamber with mu metal for shielding of ambient magnetic fields. The RFA includes a faceplate with holes drilled in it to mimic the vacuum chamber, a high efficiency (nominally 92%) retarding grid, and a collector. We are able to independently control the voltage and read the current on the collector, grid, and faceplate, as well as a top ring surrounding the faceplate. To do a measurement with this system, we set the electron gun to a specific energy, and adjust the deflection and focusing of the gun until the beam just covers the faceplate (i.e. until no current is observed on the top ring). We can then study the response of the RFA as a function of gun energy. Fig. 22 shows a series of retarding voltage scans done with our bench setup at different electron gun energies, and compares them to predictions from the particle tracking model. A few things are worth noting about these measurements:

- The collector signal is mostly flat for a retarding voltage between 0 and the gun energy, as expected for a monoenergetic beam.
- When the grid voltage is positive, there is a strong enhancement of the signal, caused by the production of low energy secondary electrons in the faceplate holes (described above).
- With +100 V on the grid (on the left side of the plots), the signal drops back down somewhat. This is because secondaries produced on the collector (which is also set to +100 V) are now able to escape.
- If the RFAs were ideal, the collector signal would drop to zero when the retarding voltage exceeds the gun energy. In the 100 eV and 200 eV scans, the signal does not immediately vanish, but drops off steadily, reaching zero current at -120 V and -230 V respectively. This effect is caused by focusing of the electrons by the non-ideal field of the grid, which allows electrons with energy slightly lower than the retarding voltage to slip by. This effect has also been observed in studies of RFA performance done at FNAL [10].

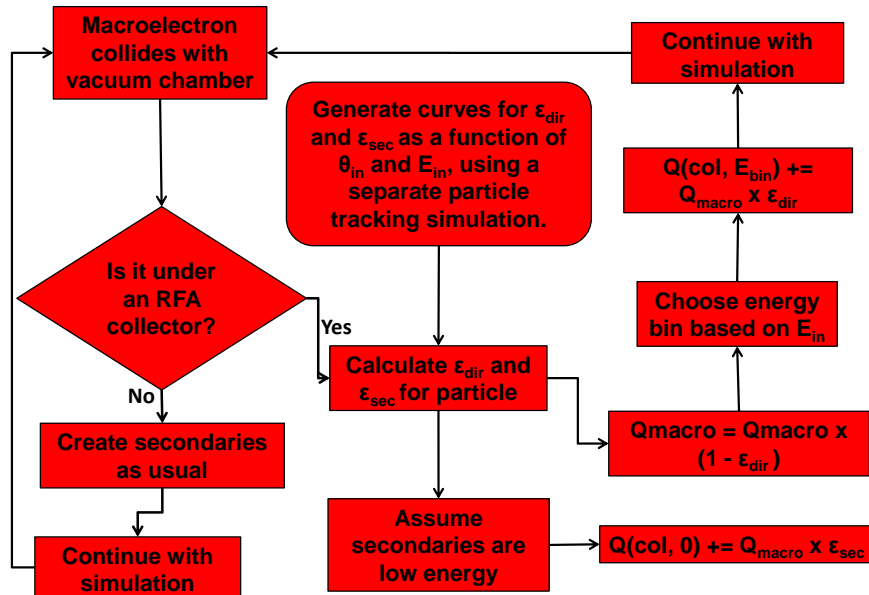


FIG. 19: Conceptual flowchart of the RFA model in POSINST. The charge deposited in the collector is binned by energy and collector number ($Q(col, E_{bin})$). The magnitude of this quantity depends on the macroelectron charge (Q_{macro}) and the efficiency of the RFA (ϵ_{dir}), which in turn depends on the incident particle energy (E_{in}) and angle (θ_{in}). In addition, the macroelectron can generate low energy “secondary” charge ($Q(col, 0)$), depending on the secondary efficiency (ϵ_{sec}). Charge that enters the RFA is removed from the macroelectron.

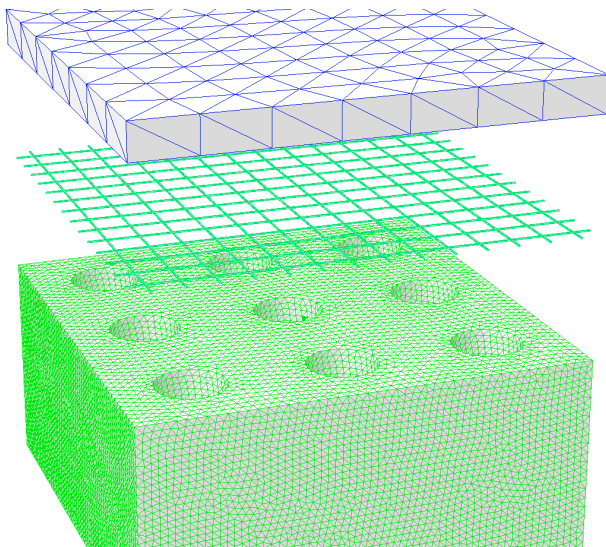


FIG. 20: Opera 3D model of a typical drift RFA, showing (from top to bottom) the collector, thin retarding grid, and faceplate/vacuum chamber.

The simulation matches all important features of the data, including the enhancement at positive voltage and the non-ideal energy cutoff. The agreement is nearly perfect for 100eV, and 200eV, but the simulation slightly underestimates the collector signal at positive voltage for

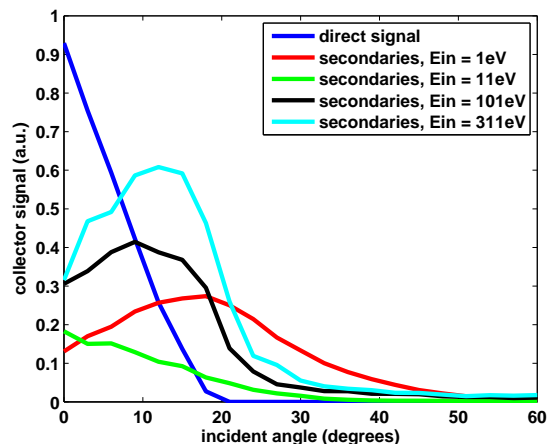


FIG. 21: Simulated collector current caused by a uniform beam of electrons incident on the thin RFA model. The direct signal is determined only by the angular acceptance of the beam pipe holes. The “secondary” signal is caused by the production of (low energy) secondary electrons in the beam pipe holes and retarding grid, and depends on the energy of the incident electrons.

500eV and 1keV. This aspect of the data is not understood, but could be due to a change in the beam profile at high gun energy, which is not included in our model. Nonetheless, the agreement between the measurement

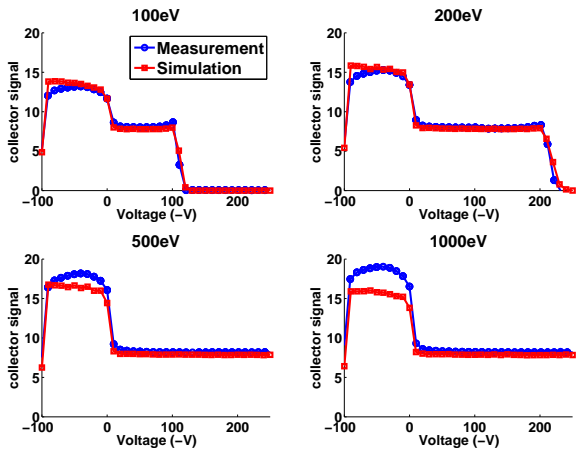


FIG. 22: Comparison of bench measurement and simulation, with electron gun energy 100 eV (top left), 200 eV (top right), 500 eV (bottom left), and 1 keV (bottom right).

and model is excellent overall.

V. SIMULATIONS AND COMPARISON WITH MEASUREMENTS

The large quantity of RFA data obtained during the CESR-TA program necessitates a systematic method for detailed analysis. Our approach has been to take a large set of voltage scan data, and find a set of simulation parameters that bring data and simulation into as close agreement as possible. Simultaneously fitting data taken under a wide variety of beam conditions gives us confidence that our model is producing a reasonable description of the growth and dynamics of the electron cloud.

More specifically, we want to minimize χ^2 , as defined in Eq. (1). Here \mathbf{y}_d is a vector of data points, \mathbf{y}_s is a vector of simulation points, β_0 is the vector of nominal parameter values, and β is the vector of new parameter values. \mathbf{X} is the Jacobian matrix ($X_{i,j} \equiv \frac{\partial y_i}{\partial \beta_j}$), and \mathbf{W} is a diagonal matrix whose elements are $\frac{1}{\sigma_i^2}$, where σ_i is the error on data point i . Both the data and simulation can contribute to this error. The T superscript denotes the matrix transpose. Note that \mathbf{X} and \mathbf{y}_s are both evaluated at β_0 . Once a new set of parameter values is obtained, the process can be repeated with this new set as the “nominal” values. As this method uses a linear approximation for the dependence of \mathbf{y}_s on β , it will need to be iterated a few times before it converges on the actual minimum value of χ^2 .

$$\begin{aligned} \chi^2 &= \varepsilon^T \mathbf{W} \varepsilon \\ \varepsilon &\equiv \mathbf{y}_d - (\mathbf{y}_s + \mathbf{X}(\beta - \beta_0)) \end{aligned} \quad (1)$$

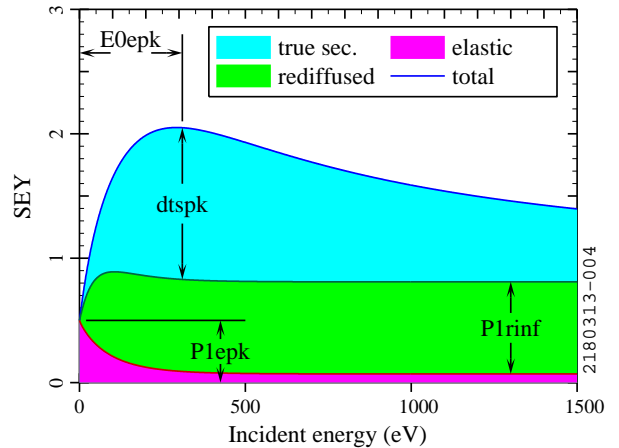


FIG. 23: Secondary electron yield as a function of energy, with important POSINST parameters indicated.

A. Simulation Parameters

There are many parameters related to primary and secondary electron emission that are relevant to this analysis. The secondary electron yield model in POSINST contains three components- “true” secondaries, which are emitted at low ($< \sim 20$ eV) energy regardless of the incident particle energy; “elastic” secondaries, which are emitted at the same energy as the incident particle; and “rediffused” secondaries, which are emitted with a uniform energy spectrum, ranging between 0 and the incident particle energy. The peak true secondary yield (characterized by the parameter $dtspk$ in POSINST) occurs for primary electrons with an incident energy (POSINST parameter $E0epk$) around 300 eV. The peak elastic yield (POSINST parameter $P1epk$) occurs at low energy (we assume 0 eV), while the rediffused yield reaches a steady state value for high energy primaries (POSINST parameter $P1rinf$). Fig. 23 shows a typical SEY curve, and indicates how each of these parameters contributes to the total secondary yield (POSINST parameter $dtotpk$).

Another relevant secondary emission parameter is the “shape parameter” $powts$, which determines the shape of the true secondary curve about its peak. This parameter was not fitted, but was obtained from in-situ SEY measurements done in CESR [23]. The starting points for $dtspk$ and $E0epk$ were also taken from these measurements.

POSINST also makes use of several parameters that describe the properties of emitted secondary electrons. The parameters that define the true-secondary emission energy distribution were chosen to give a peak emission energy of 1.5 eV, based on RFA measurements done in a dipole [28]. Secondaries are emitted with angular distribution $\frac{\partial N}{\partial \theta} \propto \sin(\theta) \cos(\theta)$, where θ is the angle relative to normal.

TABLE V: Summary of relevant POSINST parameters. The last column indicates whether the parameter was used in fits always (A), in some cases (S), or never (N).

Parameter	Description	Fit?
dtspk	True secondary yield	A
P1epk	Elastic yield	S
P1rinf	Rediffused yield	S
dtotpk	Total peak yield	N ^a
E0epk	Peak yield energy	N
powts	Shape parameter	N
queffp	Quantum efficiency	A

^aEqual to the sum of the three SEY components at peak energy

The model for photoelectron emission in POSINST is simpler than the secondary model, but still involves several important parameters. The most significant of these is the quantum efficiency (**queffp**). In addition, we have found that in order to have any RFA signal for a high current electron beam simulation, a high energy component in the photoelectron energy spectrum is required. This is accomplished by using a Lorentzian photoelectron energy distribution (which has been observed in some measurements [29]), with a low peak energy (5 eV), and a width that scales with the average photon energy incident at the RFA position. For example, for an electron beam at Q15E, the width is 12 eV for a 2.1 GeV beam, and 150 eV for a 5.3 GeV beam. The drift RFA data does not constrain the exact shape of the distribution. Measurements with a shielded pickup detector [19] provide a method to probe these parameters in more detail.

The photon flux and azimuthal distribution at the RFA are determined by a 3 dimensional simulation of photon production and reflection [30], which includes diffuse scattering and a realistic model of the CESR vacuum chamber geometry. The quantum efficiency was allowed to be different for different beam energies and species, since it will in general depend on photon energy [31].

Generally speaking, **dtspk** and **queffp** need to be included in the fitting procedure to get good agreement with the RFA data. Other strong parameters include **P1epk**, **P1rinf**, and **powts**, but they are highly correlated with each other (i.e. have similar effects on the RFA simulation), so only one of the three is needed. For the uncoated chambers (Al and Cu), we varied **P1epk**. For the coated chambers (aC, TiN, DLC, NEG), we found this parameter usually tended towards 0 in the fits, so we assumed a low value (.05), and varied **P1rinf** instead. In addition, the analysis uses one arbitrary parameter: a “chamber hole SEY,” which is an overall scaling of the effect of secondaries generated in the RFA on the low energy signal (Fig. 21). The fitted values for this parameter are within the expected range; a typical number for the effective hole SEY is on the order of 1.5.

Table V summarizes the POSINST parameters most relevant to our analysis and indicates whether the parameter was used in the fits.

B. Fitting the Data

In performing the χ^2 analysis, the choice of which data to fit and which simulation parameters to vary are both important. We want a set of parameters that have a strong effect on the simulations, and a set of voltage scans that determine these parameters as independently as possible. For example, the true secondary yield is highest for ~ 300 eV electrons, so it is best determined by data taken under beam conditions where a typical electron energy is on that order. This tends to mean short bunch spacing and moderately high current. The elastic yield mainly affects the decay of the cloud, when most of the cloud particles have low energy. It is best derived from data where the cloud is repeatedly generated and allowed to decay, i.e. for large bunch spacing. The quantum efficiency is most significant in regimes where secondary emission is less important, namely for low current data. Table VI gives a list of data sets used in one round of fitting, and indicates which parameter was best determined by each.

Several sources of error can complicate the analysis, and must be added (in quadrature) when constructing the error matrix (**W** in Eq. (1)). They are listed below. For the purpose of comparison, a typical signal in the 15E/W RFAs is on the scale of 100’s of nA.

- Noise in the measurements (typically quite small, a few tenths of a nA)
- Statistical errors in simulations. This can be reduced by increasing the number of macroelectrons used in the simulation, at the cost of increased run time. Typical values are on the order of a few nA.
- A general error of 10% was added to account for systematic uncertainties in the data. One such uncertainty is unevenness in bunch currents along the train, which is not accounted for in the simulation. The choice of 10% is somewhat arbitrary, but was chosen to reflect our confidence in the repeatability of the measurements.
- We have observed a slow drift of baseline (zero current value) in measurements, on the order of $\sim .2\%$ of full scale. This amounts to ~ 20 nA on the lowest gain setting, and $\sim .02$ nA on the highest one (2 nA for a typical case).
- An extra 20% error was added to the signal in the simulation caused by beam pipe hole secondaries, to account for uncertainty in the modeling of this phenomenon. Again this choice is somewhat arbitrary.
- Since the gradient for the Jacobian matrix (**X**) is determined by simulation, it will also have an associated error. This cannot be included in the **W** matrix, because it will be different for each parameter. However, it can still be calculated, and its effect on the final parameter errors can be estimated.

TABLE VI: List of beam conditions used for one round of fitting (15W Al chamber, May 2010), and which parameter they most strongly determined

Bunches	Bunch current	Bunch Spacing	Beam Energy	Parameter
45 e ⁻	2.89 mA	4 ns	5.3 GeV	dtspk
45 e ⁺	2.3 mA	14 ns	2.1 GeV	dtspk
20 e ⁺	7.5 mA	14 ns	2.1 GeV	dtspk
20 e ⁻	2.8 mA	14 ns	5.3 GeV	dtspk
20 e ⁺	2.8 mA	4 ns	4 GeV	dtspk
9 e ⁻	3.78 mA	280 ns	2.1 GeV	P1epk
20 e ⁺	10.75 mA	14 ns	5.3 GeV	P1epk
9 e ⁺	3.78 mA	280 ns	2.1 GeV	P1epk
9 e ⁺	3.78 mA	280 ns	4 GeV	P1epk
9 e ⁺	4.11 mA	280 ns	5.3 GeV	P1epk
45 e ⁺	0.75 mA	14 ns	5.3 GeV	queffp
45 e ⁻	1.25 mA	4 ns	5.3 GeV	queffp
45 e ⁺	0.75 mA	14 ns	4 GeV	queffp
45 e ⁺	0.75 mA	14 ns	2.1 GeV	queffp
45 e ⁻	2 mA	14 ns	2.1 GeV	queffp

C. Results

Figs. 24 and 25 show some of the results of the χ^2 analysis, for an uncoated aluminum drift chamber. The plots compare both the transverse and energy distribution of the data and fitted simulation. The error bars shown reflect all of the uncertainties described above. Overall the two are in good agreement for a wide variety of beam conditions. The biggest discrepancy between data and simulation occurs for high current electron beam data. These are the conditions most likely to produce ion effects, which are not included in our model, and may be leading to this discrepancy.

The covariance matrix for the parameters is $(\mathbf{X}^T \mathbf{W} \mathbf{X})^{-1}$. The standard errors on each parameter are equal to the square root of the diagonal elements of this matrix. These errors are one dimensional 68% confidence intervals for each parameter individually, without regard for the values of the other parameters. The covariance matrix is multiplied by the “ χ^2 per degree of freedom” ($\frac{\chi^2}{n-p}$, where n is the number of data points and p is the number of parameters fitted). Effectively this scales up the uncertainty on the data points, to include (in a somewhat ad hoc manner) any errors that have been left out of the analysis. The values listed for the error bars also include an estimate of the uncertainty introduced by errors in the Jacobian matrix, which is added in quadrature to the standard error. The correlation coefficient of two parameters is defined as $\rho \equiv \frac{C_{i,j}}{\sqrt{C_{i,i} \times C_{j,j}}}$, where $C_{i,j}$ is the i, j th element of the covariance matrix. In general the correlation between parameters is significant. For example, in the fits shown in Figs. 24 and 25, $\rho = .42$ for dtspk and P1epk, $.22$ for dtspk and queffp, and $.31$ for P1epk and queffp.

It should be noted that, with the number of parameters involved in the analysis, it is impossible to say whether we have arrived at the global minimum value of χ^2 in

parameter space. Nonetheless, the ability of this method to achieve a good fit for data taken under a wide variety of beam conditions strongly implies that the primary and secondary emission models used are reproducing reality to a reasonable degree.

The best fit values and 68% confidence intervals for the aluminum chamber fit are shown in Table VII. This chamber was installed in the Q15W location (see Section III), and the fit used data taken during May 2010 (listed in Table VI). Tables VIII through XII give the best fit values for (fully processed) aC, TiN, DLC, bare Cu, and NEG, respectively. In these tables, the quantum efficiency best fit values are given for positron beam data; the complete set of quantum efficiency fits is shown in Table XIII.

Each of these results represents a fit using to a series of voltage scans done during one CESR-TA machine studies run, typically within a few days of each other. Several such fits were done for most of the chambers, and the results were usually found to be consistent, with a few exceptions. In particular, some of the fits for aC showed a higher quantum efficiency, but somewhat lower rediffused yield. This may represent a different state of processing of the chamber. In the results presented below, the fit with the lowest χ^2 for each chamber was chosen.

Some of the more significant features of these results include:

- The true secondary yield (dtspk) for the uncoated Al chamber was found to be very high (> 2). All of the coated chambers (aC, TiN, DLC, and NEG) had much lower values, corresponding in all cases to a peak SEY $\leq .9$. The value for TiN and DLC in particular are very low, implying a peak SEY on the order of 0.7.
- The DLC fit also required a very low value for the “chamber hole SEY” parameter described above. This could be understood as compensating for a

TABLE VII: Best fit parameters- Q15W aluminum chamber, May 2010

Parameter	Base Value	Final Value
dtspk	1.37	$2.08 \pm .09$
P1epk	.5	$.36 \pm .03$
P1rinf	.2	.2
dtotpk	1.59	$2.3 \pm .1$
E0epk	280eV	280eV
powts	1.54	1.54
queffp, 5.3GeV	.1	$.10 \pm .01$
queffp, 2.1GeV	.1	$.11 \pm .01$

suppression of the low energy signal due to charging of the chamber (see Section III B 2).

- The best fit values for quantum efficiency were also lower for the coated chambers. Amorphous carbon consistently had the lowest values, less than 5% for all cases.
- Since we don't have a direct measurement of the SEY curve for NEG, the initial values for the parameters were (somewhat arbitrarily) taken from TiN. The fitted values for NEG indicate a much higher rediffused yield than the other coated chambers.
- The best fit value for the elastic yield was found to be low for both uncoated (Al and Cu) chambers. This parameter was not varied for the coated chambers, but the fits were generally found to be better if a very low value (.05) was assumed. For these chambers, the rediffused yield was varied instead.
- In most cases, the quantum efficiency fit was significantly higher for 5.3 GeV than for 2.1 GeV.

The SEY curves generated by the best fit parameters for each chamber are shown in Fig. 26.

TABLE VIII: Best fit parameters- Q15E aC coated chamber, December 2010

Parameter	Base Value	Final Value
dtspk	.76	$.59 \pm .05$
P1epk	.05	.05
P1rinf	.2	$.30 \pm .05$
dtotpk	.98	$.91 \pm .07$
E0epk	300eV	300eV
powts	1.77	1.77
queffp, 5.3GeV	.1	$.046 \pm .005$
queffp, 2.1GeV	.1	$.036 \pm .005$

VI. CONCLUSIONS

Retarding field analyzers have been installed in drift regions around CESR, and a great deal of electron cloud data has been collected with them. These data have been used to directly compare the efficacy of various electron

TABLE IX: Best fit parameters- Q15W TiN-coated chamber, December 2010

Parameter	Base Value	Final Value
dtspk	.73	$.59 \pm .03$
P1epk	.05	.05
P1rinf	.2	$.13 \pm .03$
dtotpk	.85	$.75 \pm .04$
E0epk	370eV	370eV
powts	1.32	1.32
queffp, 5.3GeV	.1	$.089 \pm .007$
queffp, 2.1GeV	.1	$.050 \pm .004$

TABLE X: Best fit parameters- Q15E DLC coated chamber, April 2012

Parameter	Base Value	Final Value
dtspk	.76	$.48 \pm .06$
P1epk	.05	.05
P1rinf	.2	$.20 \pm .06$
dtotpk	.98	$.70 \pm .08$
E0epk	190eV	190eV
powts	1.77	1.77
queffp, 5.3GeV	.1	$.099 \pm .011$
queffp, 2.1GeV	.1	$.042 \pm .006$

TABLE XI: Best fit parameters- Q14E bare Cu chamber, May 2010

Parameter	Base Value	Final Value
dtspk	.82	$.81 \pm .05$
P1epk	.5	$.22 \pm .07$
P1rinf	.28	.28
dtotpk	1.12	$1.11 \pm .09$
E0epk	375eV	375eV
powts	1.38	1.38
queffp, 5.3GeV	.1	$.15 \pm .03$
queffp, 2.1GeV	.1	$.025 \pm .008$

TABLE XII: Best fit parameters- L3 NEG-coated chamber, December 2010

Parameter	Base Value	Final Value
dtspk	.73	$.42 \pm .07$
P1epk	.05	.05
P1rinf	.2	$.46 \pm .05$
dtotpk	.97	$.90 \pm .09$
E0epk	370eV	370eV
powts	1.32	1.32
queffp, 5.3GeV	.1	$.14 \pm .02$
queffp, 2.1GeV	.1	$.03 \pm .01$

cloud mitigating coatings. Detailed models of our RFAs have been developed, and integrated into the cloud simulation code POSINST, allowing for analysis on a more fundamental level. This has enabled the calculation of best fit simulation parameters, which describe the primary and secondary electron emission characteristics of each material in situ.

Both direct measurement and simulation show that all

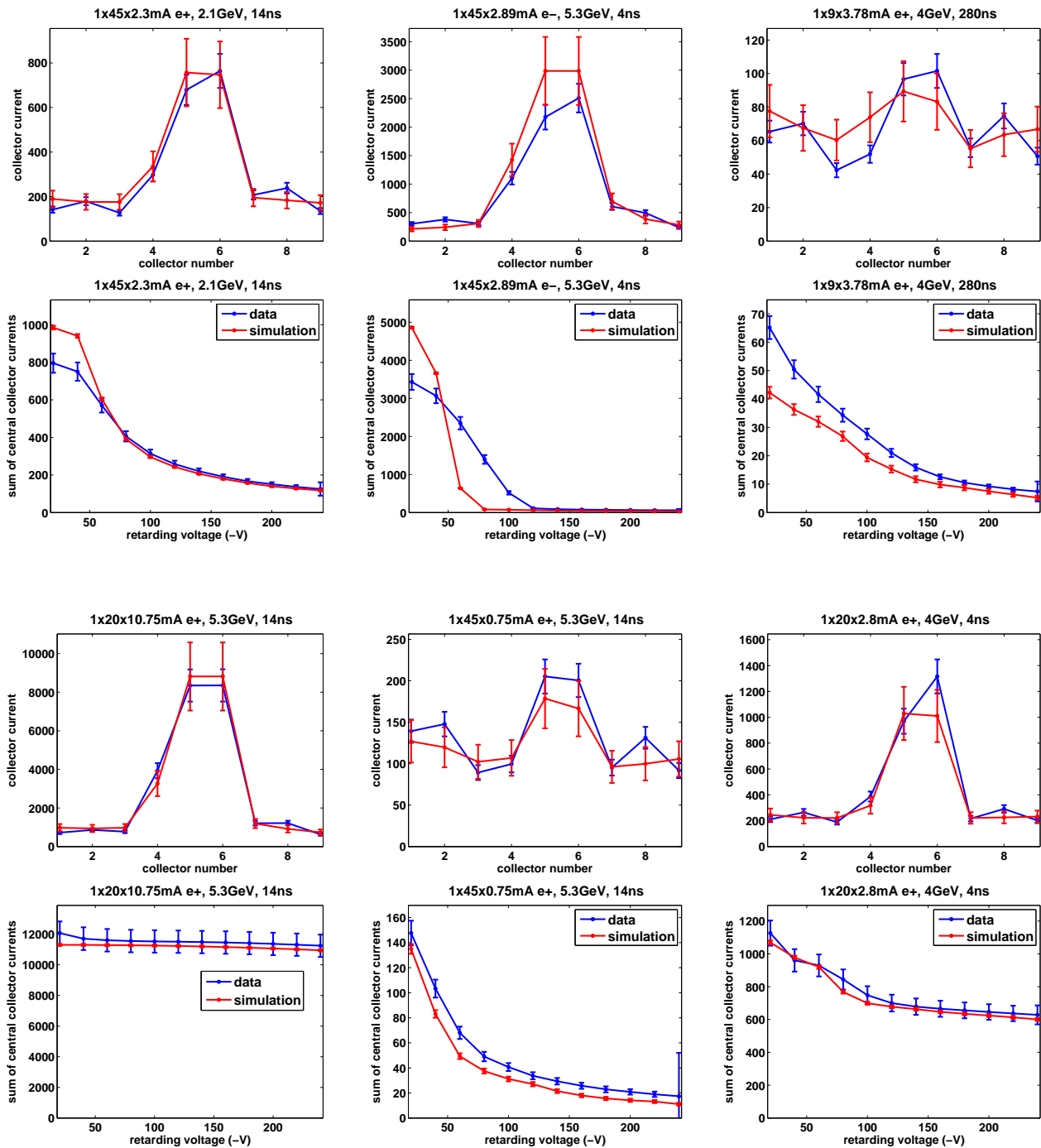


FIG. 24: Comparison of Q15W Al RFA data and simulation, using best fit parameters (Table VII). The top plots show the total signal across the 9 RFA collectors (with +50 V on the grid); the bottom plots show the signal in the central three collectors vs retarding voltage.

of the coatings tested are effective at suppressing the cloud. The fits indicate that TiN and DLC have especially low secondary yields, while aC has the lowest quantum efficiency. Also, with the possible exception of diamond-like carbon, the coatings show mostly stable behavior over the long term.

Electronic properties of material surfaces, such as

quantum efficiency and secondary emission yield, are traditionally measured employing dedicated, well-controlled laboratory devices applied to clean, smooth surfaces. The analysis presented here, on the other hand, presents the determination of several model parameters via a simultaneous, multi-parameter fit to data obtained with RFAs installed in the CESR-TA vacuum chamber. Thus, while

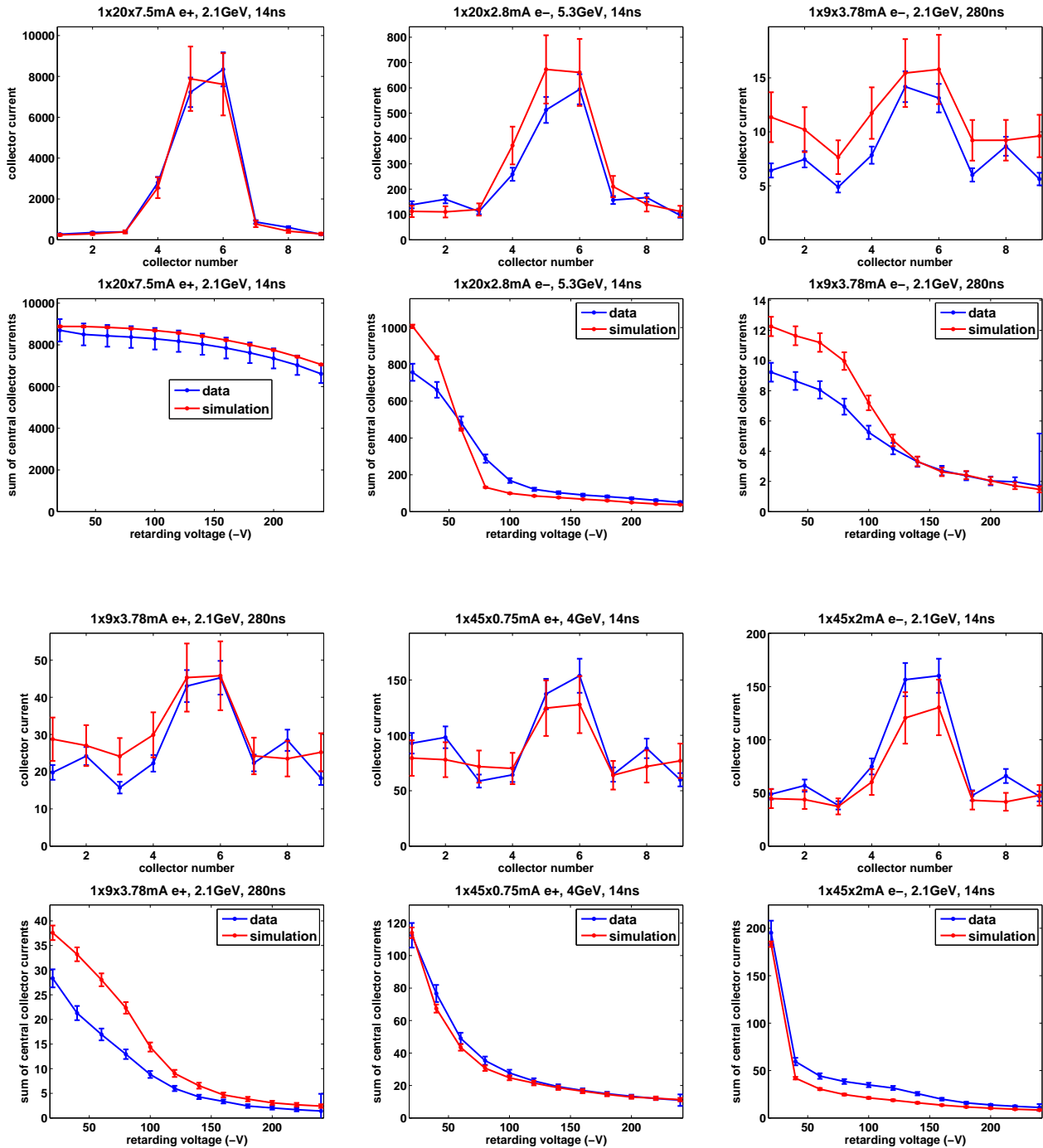


FIG. 25: Comparison of Q15W Al RFA data and simulation, using best fit parameters (Table VII). The top plots show the total signal across the 9 RFA collectors (with +50 V on the grid); the bottom plots show the signal in the central three collectors vs retarding voltage.

none of the above-mentioned parameters is determined with great precision, our exercise amounts to a more global fit to the model, and yields reasonable values for the parameters. In combination with many other kinds of measurements (published separately [19, 23, 30, 32]) within the CESR-TA program, our results lend validity to the electronic model embodied in the simulation code.

Our approach has the additional advantage that it allows the assessment of the performance of various chamber materials vis-a-vis the electron-cloud problem for actual chamber surfaces within a realistic storage ring environment. As such, our analysis takes intrinsic account of such issues as surface roughness, material composition, and beam conditioning. Given the ubiquitousness of the

TABLE XIII: Table of best fit quantum efficiencies (in percent)

Material	2.1 GeV, e ⁺	2.1 GeV, e ⁻	4 GeV, e ⁺	5.3 GeV, e ⁺	5.3 GeV, e ⁻	Average
Al	11.3 ± 1.4	8.0 ± 1.1	10.0 ± 1.2	10.3 ± 1.2	10.5 ± 1.4	10.0
Cu	2.5 ± .8	4.7 ± .7	15.0 ± 2.0	15.3 ± 2.8	12.1 ± 1.8	9.9
TiN	4.9 ± .2	-	-	8.9 ± .7	5.0 ± .4	6.3
aC	3.6 ± .5	-	-	4.6 ± .6	4.9 ± .6	4.4
DLC	4.5 ± .6	7.1 ± .6	-	9.1 ± 1.1	7.1 ± .6	7.0
NEG	2.9 ± .9	-	-	14 ± 2	-	8.5

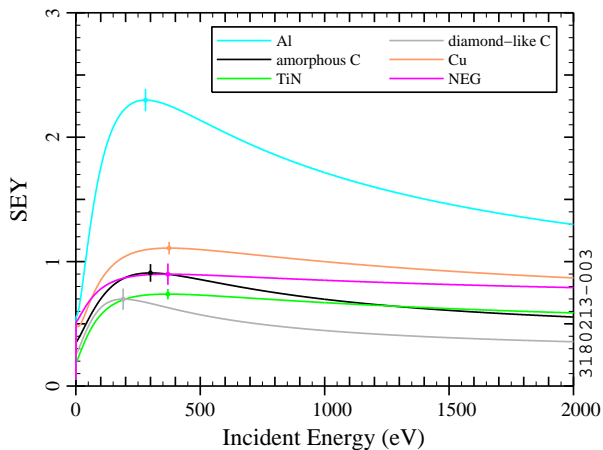


FIG. 26: Secondary electron yield curves generated by the best fit parameters for each chamber (Tables VII - XII). Error bars are shown for the peak yield values.

electron-cloud effect, our results are directly and immediately applicable to other high-energy or high-intensity storage rings, whether lepton or hadron.

Acknowledgments

The results presented in this paper were made possible by the hard work of the CESR-TA collaboration, especially L. Bartnik, M.G. Billing, J.V. Conway, J.A. Crittenden, M. Forster, S. Greenwald, Y. Li, X. Liu, R.E. Meller, S. Roy, S. Santos, R.M. Schwartz, J. Sikora, and C.R. Strohmman. We are also grateful to S. Calatroni and G. Rumolo at CERN for providing us with the aC coated chambers, and S. Kato at KEK for the DLC chamber.

Finally, the authors would like to thank D. Rubin at Cornell for his advice and guidance, and M. Furman at LBNL for his support with the POSINST simulation code.

- [1] M. Furman, in *Proceedings of ECLLOUD 2012: 5th International Workshop on Electron-Cloud Effects, La Biodola, Elba, Italy* (in press).
- [2] Y. Cai, M. Pivi, and M. A. Furman, *Phys. Rev. ST Accel. Beams* **7**, 024402 (2004).
- [3] C. Yin Vallgren, G. Arduini, J. Bauche, S. Calatroni, P. Chigiato, K. Cornelis, P. Costa Pinto, B. Henrist, E. Métral, H. Neupert, et al., *Phys. Rev. ST Accel. Beams* **14**, 071001 (2011).
- [4] Y. Susaki and K. Ohmi, in *Proceedings of the 2010 International Particle Accelerator Conference, Kyoto, Japan* (2010), pp. 1545–1547, URL <http://accelconf.web.cern.ch/AccelConf/IPAC10/papers/tupeb014.pdf>.
- [5] M. A. Furman, M. Pivi, K. C. Harkay, and R. A. Rosenberg, in *Proceedings of the 2001 Particle Accelerator Conference, Chicago, IL*, edited by P. Lucas and S. Webber (2001), pp. 679–681, URL <http://accelconf.web.cern.ch/AccelConf/p01/PAPERS/FOAB004.PDF>.
- [6] N. Eddy, J. Crisp, I. Kourbanis, K. Seiya, B. Zwaska, and S. De Santis, in *Proceedings of the 2009 Particle Accelerator Conference, Vancouver, BC* (2009), pp. 1967–1969, URL <http://accelconf.web.cern.ch/AccelConf/PAC2009/papers/we4grc02.pdf>.
- [7] O. Domnguez, K. Li, G. Arduini, E. Metral, G. Rumolo, and F. Zimmermann, *Phys. Rev. ST Accel. Beams* **16**, 011003 (2013).
- [8] M. T. F. Pivi, L. Wang, T. Demma, S. Guiducci, Y. Suetsugu, K. Shibata, K. Ohmi, G. Dugan, M. Palmer, J. A. Crittenden, et al., in *Proceedings of the 2011 International Particle Accelerator Conference, San Sebastián, Spain* (2011), pp. 1063–1065, URL <http://accelconf.web.cern.ch/AccelConf/IPAC2011/papers/tupc030.pdf>.
- [9] R. A. Rosenberg and K. C. Harkay, *Nucl. Instrum. Methods Phys. Res.* **A453**, 507 (2000).
- [10] C. Y. Tan, K. L. Duel, and R. M. Zwaska, in *Proceedings of the 2009 Particle Accelerator Conference, Vancouver, BC* (2009), pp. 3540–3542, URL <http://accelconf.web.cern.ch/AccelConf/PAC2009/papers/th5rfp041.pdf>.
- [11] M. T. F. Pivi, J. S. T. Ng, F. Cooper, D. Kharakh, F. King, R. E. Kirby, B. Kuekan, C. M. Spencer, T. O. Raubenheimer, and L. F. Wang, *Nucl. Instrum. Methods Phys. Res.* **A621**, 33 (2010).
- [12] K. Kanazawa, H. Hukuma, H. Hisamatsu, and Y. Suetsugu, in *Proceedings of the 2005 Particle Accelerator Conference, Knoxville, TN*, edited by C. Horak (2005), pp. 1054–1056, URL <http://accelconf.web.cern.ch/AccelConf/p05/PAPERS/FPAP007.PDF>.
- [13] D. Rubin, in *Proceedings of ECLLOUD 2010: 49th ICFA Advanced Beam Dynamics Workshop on Electron Cloud Physics, Ithaca, NY*, edited by K. Smolenski (in press),

Paper OPR06.

- [14] F. Le Pimpec, R. E. Kirby, F. King, and M. Pivi, *Nucl. Instrum. Methods Phys. Res.* **A551**, 187 (2005).
- [15] S. Kato and M. Nishiwaki, in *Proceedings of ELOUD 2010: 49th ICFA Advanced Beam Dynamics Workshop on Electron Cloud Physics, Ithaca, NY*, edited by K. Smolenski (in press), Paper MIT00.
- [16] Y. Suetsugu, K. Kanazawa, K. Shibata, H. Hisamatsu, K. Oide, F. Takasaki, R. V. Dostovalov, A. Krasnov, K. V. Zolotarev, E. S. Konstantinov, et al., *Nucl. Instrum. Methods Phys. Res.* **A554**, 92 (2005).
- [17] Tech. Rep. CLNS-12-2084, LEPP, Cornell University, Ithaca, NY (2012), URL <http://www.lns.cornell.edu/public/CLNS/2012/CLNS12-2084/>.
- [18] M. A. Palmer, M. G. Billing, J. R. Calvey, G. W. Codner, S. Greenwald, Y. Li, X. Liu, J. A. Livezey, R. E. Meller, R. M. Schwartz, et al., in *Proceedings of the 2009 Particle Accelerator Conference, Vancouver, BC* (2009), pp. 3510–3512, URL <http://accelconf.web.cern.ch/AccelConf/PAC2009/papers/th5rfp030.pdf>.
- [19] J. A. Crittenden, Y. Li, X. Liu, M. A. Palmer, J. P. Sikora, S. Calatroni, and G. Rumolo, in *Proceedings of the 2011 Particle Accelerator Conference, New York, NY* (2011), pp. 1752–1754, URL <http://accelconf.web.cern.ch/AccelConf/PAC2011/papers/wep142.pdf>.
- [20] O. Gröbner, in *Proceedings of the X International Conference on High Energy Accelerators, Protvino, USSR, 1977*, edited by Y. M. Ado, A. G. Afonin, V. I. Gridasov, A. F. Dunaitsev, E. A. Mjae, and A. A. Naumov (1977), pp. 277–282.
- [21] K. C. Harkay, L. Loiacono, and R. A. Rosenberg, in *Proceedings of the 2003 Particle Accelerator Conference, Portland, OR*, edited by J. Chew, P. Lucas, and S. Weber (2003), pp. 3183–3185, URL <http://accelconf.web.cern.ch/AccelConf/p03/PAPERS/RPPG002.PDF>.
- [22] R. Cimino, M. Commisso, D. R. Grosso, T. Demma, V. Baglin, R. Flammini, and R. Larciprete, *Phys. Rev. Lett.* **109**, 064801 (2012).
- [23] J. Kim, D. Asner, J. Conway, S. Greenwald, Y. Li, V. Medjidzade, T. Moore, M. Palmer, and C. Strohman, in *Proceedings of ELOUD 2010: 49th ICFA Advanced Beam Dynamics Workshop on Electron Cloud Physics, Ithaca, NY*, edited by K. Smolenski (in press).
- [24] J. A. Crittenden and J. P. Sikora, in *Proceedings of ELOUD 2012: 5th International Workshop on Electron-Cloud Effects, La Biodola, Elba, Italy* (in press).
- [25] M. A. Furman and G. R. Lambertson, in *Proceedings of MBI97: International Workshop on Multibunch Instabilities in Future Electron and Positron Accelerators, Tsukuba, Japan, 1997*, edited by Y. H. Chin (1997), KEK Proceedings 97-17, p. 170, URL <http://escholarship.org/uc/item/2bt512wj>.
- [26] M. A. Furman, Tech. Rep. LHC Project Report 180/LBNL-41482/CBP Note 247, CERN, Geneva, Switzerland (1998), URL <http://wwwslap.cern.ch/collective/electron-cloud/furman/LHCpr180.pdf>.
- [27] M. A. Furman and M. T. F. Pivi, *Phys. Rev. ST Accel. Beams* **5**, 124404 (2002).
- [28] J. R. Calvey, M. G. Billing, J. V. Conway, G. Dugan, S. Greenwald, Y. Li, X. Liu, J. A. Livezey, J. Makita, R. E. Meller, et al., in *Proceedings of the 2011 International Particle Accelerator Conference, San Sebastián, Spain* (2011), pp. 796–798, URL <http://accelconf.web.cern.ch/AccelConf/IPAC2011/papers/mops083.pdf>.
- [29] R. Cimino, I. R. Collins, and V. Baglin, *Phys. Rev. ST Accel. Beams* **2**, 063201 (1999).
- [30] G. Dugan and D. Sagan, in *Proceedings of ELOUD 2010: 49th ICFA Advanced Beam Dynamics Workshop on Electron Cloud Physics, Ithaca, NY*, edited by K. Smolenski (in press).
- [31] L. Boon and K. Harkay, in *Proceedings of ELOUD 2012: 5th International Workshop on Electron-Cloud Effects, La Biodola, Elba, Italy* (in press).
- [32] D. L. Kreinick, J. A. Crittenden, G. Dugan, M. A. Palmer, G. Ramirez, R. L. Holtzapple, M. Randazzo, M. A. Furman, and M. Venturini, in *Proceedings of the 2011 Particle Accelerator Conference, New York, NY* (2011), pp. 1680–1682, URL <http://accelconf.web.cern.ch/AccelConf/PAC2011/papers/wep108.pdf>.